ADVANCED FUNCTIONAL MATERIALS
www.afm-journal.de

Enhanced Elastic Migration of Magnesium Cations in alpha-Manganese Dioxide Tunnels Locally Tuned by Aluminium Substitution

Yaxi Ding, Siwen Zhang, Jiazhuo Li, Ying Sun, Bosi Yin, Hui Li, Yue Ma, Zhiqiao Wang, Hao Ge, Dawei Su,* and Tianyi Ma**

The harsh conditions of large hydrated ion radius of Mg^{2+} cations and the strong electrostatic interaction with the host material put forward higher requirements for high-performance aqueous magnesium ion (Mg^{2+}) energy storage devices. Herein, substituted aluminium ions (Al^{3+}) doped α-MnO_2 materials are prepared. The introduction of Al^{3+} cations adjust the local chemical environment inside the tunnel structure of α-MnO_2 and precisely regulates the diffusion behavior of inserted Mg^{2+} cations. The shortened oxygens' distance and abundant oxygen defects result in a substantially enhanced elastic migration pattern of Mg^{2+} cations driven by strengthened electrostatic attraction, which brings the lower diffusion energy barrier, improved reaction kinetics, and adaptive volume expansion as evidenced by Climbing Image-Nudged Elastic Band density function theory calculations coupled with experimental confirmation in X-ray photoelectron spectroscopy, electron paramagnetic resonance, and galvanostatic intermittent titration technique. As a result, this rationally designed cathode exhibits a high reversible capacity of 197.02 mAh g^{-1} at 0.1 A g^{-1} and stable cycle performance of 2500 cycles with 82% retention. These parameters are among the best of Mg-ion capacitors reported to date. This study offers a detailed insight into the local tunnel structure tunning effect and opens up a new path of modification for tunnel-type structural materials.

1. Introduction

Metallic magnesium cations as charge carriers for energy storage devices were first reported by Gregory in the 1990s.[1] Theoretically, the magnesium ion with the same ionic radius as a lithium-ion can deliver twice as many electrons as univalent cations (lithium-ion or sodium-ion).[2–4] Concurrently, magnesium has abundant natural sources and low production costs.[5] Rechargeable energy storage devices based on magnesium as a substitute for current commercial lithium-ion batteries have gradually become a hot topic in recent years. However, magnesium ions continue to suffer from delayed solid-state diffusion and significant polarization issues as a result of the divalent cation's strong coulombic interaction with the host.[6] Leveraging aqueous electrolytes with high ionic conductivity instead of organic electrolytes can alleviate the sluggish ion diffusion kinetics.[7] Such

Y. Ding, S. Zhang, J. Li, Y. Sun, B. Yin
Institute of Clean Energy Chemistry
Key Laboratory for Green Synthesis and Preparative Chemistry of Advanced Material
College of Chemistry
Liaoning University
Shenyang 110036, P. R. China
E-mail: zhangsiwen@lnu.edu.cn

H. Li, T. Ma
School of Science
RMIT University
Melbourne, VIC 3000, Australia
E-mail: tianyi.ma@rmit.edu.au

The ORCID identification number(s) for the author(s) of this article can be found under https://doi.org/10.1002/adfm.202210519.

DOI: 10.1002/adfm.202210519

Y. Ma, Z. Wang
State Key Laboratory of Solidification Processing
Center for Nano Energy Materials
School of Materials Science and Engineering
Shaanxi Joint Laboratory of Graphene
Northwestern Polytechnical University
Xi'an 710072, P. R. China

H. Ge
College of Energy and Environment
Shenyang Aerospace University
Shenyang 110136, P. R. China

D. Su
School of Mathematical and Physical Sciences
Faculty of Science
University of Technology Sydney
Sydney, NSW 2007, Australia
E-mail: dawei.su@uts.edu.au

initiatives can help alleviate the drawbacks that organic electrolytes bring, such as poor electrochemical oxidation stability, being flammable, and being hazardous to living organisms.[8] In the realm of magnesium ion storage systems, there is still a barrier to discovering appropriate electrode materials to demonstrate reversible capacities, exceptional rate capabilities, and great cycling performances.

Manganese dioxide is frequently utilized in energy storage devices due to its high energy density, low cost, minimal environmental effect, and abundant natural supply.[9] Manganese dioxide is classified into four forms based on how the fundamental unit [MnO_6] octahedra are linked. The mixed-valence of Mn, high porous structure, and moderately acidic sites distinguish α-MnO_2 from other crystalline phases.[10,11] Whereas the specific capacity of most layered manganese dioxide cathodes degrades quickly because of irreversible phase shifts during a continuous cycling process, α-MnO_2 is no exception.[12–14] To overcome this obstacle, intercalation engineering of heteroatoms, particularly metal ions, is regarded as a key methodology for achieving better electrochemical behavior of α-MnO_2 cathodes.[15,16] In addition to modulating the intrinsic crystal structure of the α-MnO_2 cathode, the metal ion intercalation also optimizes the charge/ion state as well as the electronic band gap.[17,18] It generates new molecular orbitals and brings impurity energy levels into α-MnO_2.[19–21] Among various doping agents, aluminum cations are ideal due to their cost-effective and non-toxic features. Most significantly, trivalent aluminum ions can bond with O atoms to form stable aluminum chemical bonds with a high energy of 502 kJ mol^{-1}.[22] Furthermore, because the ionic radius of Al^{3+} (53.5 pm) is extremely close to that of Mn^{4+} (53 pm),[23,24] Al^{3+} is a suitable cation for the substitutional doping of manganese dioxide. Unfortunately, research into aluminum-doped manganese oxide employed in aqueous Mg-ion energy storage devices is still insufficient, and the underlying mechanism is poorly understood.

Herein, the one-step hydrothermal process was used to produce substitutional Al-doped α-MnO_2 materials. The effect of aluminum dopants on the structure as well as the electrochemical performance was discussed in detail, and the underlying reasons for the performance improvement were uncovered at the theoretical level. Adjusting the interaction between the embedded ions and the host material can benefit the electrostatic attraction of Mg^{2+} cations and decrease the Mg^{2+} diffusion barrier. The precise control of the local chemical environment in the host matrix optimizes the embedding behavior of Mg^{2+} cations, bringing rapid Mg^{2+} transportation and providing satisfactory rate performance. According to the results, the doped Al_xMnO_{2-z} has a specific capacity of 197.02 mAh g^{-1} and retains up to 82% capacity after 2500 cycles, whereas the pristine α-MnO_2 drops to 77% after 100 cycles. Based on these cathodes coupled with activated carbon anodes, an aqueous magnesium ion capacitor with an energy density of 104.86 Wh kg^{-1} was obtained. The constructed capacitor has significant application prospects and tremendous promise as a high-performance energy storage system.

2. Results and Discussion

The tunnel structured α-MnO_2 and Al^{3+} doped α-MnO_2 materials with stable Al-O bonds were synthesized, respectively. As demonstrated in **Figure 1**, Al-doped manganese oxides were synthesized by a simple one-step hydrothermal method, which is the same as the synthesis of pristine manganese oxides. The crystal structures of the as-prepared materials were characterized by X-ray diffraction (XRD, **Figure 2**a). The XRD patterns show seven major characteristic peaks at 12.8°, 18.1°, 28.8°, 37.5°, 41.9°, 49.8°, and 60.3°, respectively, associated with the (110), (200), (310), (211), (301), (411) and (521) of α-MnO_2 phase (JCPDS No. 44–0141).[25] As shown in Figure S1 (Supporting Information), the α-MnO_2 structure has one dimensional 2 × 2 (0.46 × 0.46 nm) tunnels formed by a corner and edge-sharing manganese octahedral [MnO_6] units with the I4/m space group (tetragonal crystal system). Meanwhile, mixed-valence (3^+ and 4^+) manganese centers are charge-naturally maintained by cations within the tunnel structure. Here, Energy-dispersive X-ray spectroscopy (EDS) and X-ray Photoelectron Spectroscopy (XPS) were conducted to identify the cations within the tunnel structure and help to unveil the Al^{3+} doping manner. The EDS spectra present the K Kα1 signal in both pristine and Al^{3+} doped α-MnO_2, indicating the K^+ located within the 2 × 2 tunnels, which is not surprising due to the use of the potassium permanganate precursor (Figure S2a,b, Supporting Information). Moreover, EDS mapping images (Figure S2c–g, Supporting Information) show the distribution of Al elements as well as Mn, O, and K elements in the Al-doped α-MnO_2. While Al is uniformly distributed in the

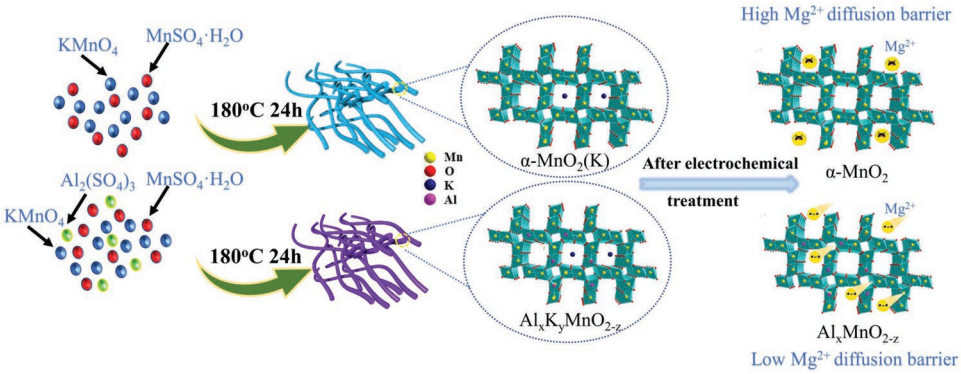

Figure 1. Schematic diagram illustrating different reaction processes of α-MnO_2 nanowires and $Al_xK_yMnO_{2-z}$ materials.

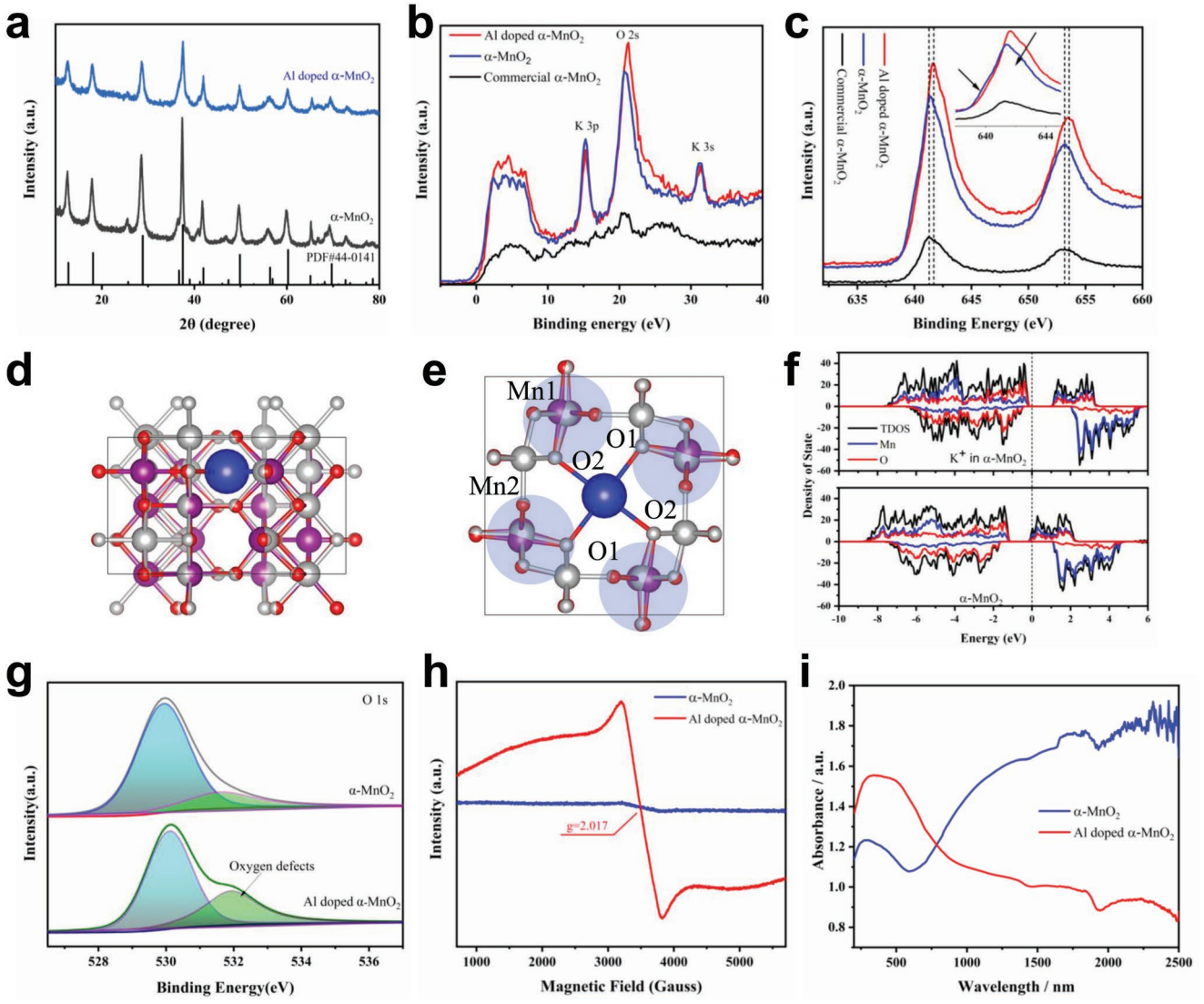

Figure 2. a) XRD patterns of α-MnO_2 and Al-doped α-MnO_2. b) XPS spectra of the fine scan spectra at the binding energy with −5–40 eV. c) High-resolved Mn 2p XPS spectra. d) side and e) top view of the relaxed structure of MnO_2 with K^+ insertion in the tunnel. The purple and red spheres represent Mn and O, respectively. The grey and white spheres are the Mn and O atoms of relaxed MnO_2 without K^+ insertion. f) The total density of states and projected density of states of the relaxed MnO_2 with and without K^+ insertion. g) O 1s XPS spectra. h) EPR spectra and i) UV–Vis absorption of the as-prepared Al-doped α-MnO_2 and α-MnO_2.

aggregated nanorods. In addition, a typical EDS line scan across the aggregated surface of the nanorods is shown in Figure S2h (Supporting Information). The presence of Mn, O, Al, and K are detected simultaneously in the volumetric region of the aggregated nanorods, which indicates that Al has been uniformly distributed in the original nanorods. The high resolved valance band region XPS spectra further confirm the K^+ within the tunnel (Figure 2b). By comparing with the commercial α-MnO_2, it is readily observed the sharp peaks of K 3p (≈ 15.3 eV) and K 3s (≈ 31.2 eV) in both pristine and Al^{3+} doped α-MnO_2 samples. The atomic ratio of the K is ≈10% quantitatively characterized by both EDS and XPS. It can be verified that the manganese centers are mixed valence, where charge neutrality is maintained by this 10 a.t. % K^+ cations. This is consistent with the high-resolution Mn 2p XPS spectra (Figure 2c). It can be seen that compared to commercial α-MnO_2, Mn $2p_{3/2}$ (located at binding energies of ≈641 eV) of the as-prepared pristine and Al-doped α-MnO_2 partial demonstrate the multiple peaks (as arrowed in the inset of Figure 2c), verifying the mixed valence feature of Mn.[26,27] As demonstrated in Figure 2d,e, when the K^+ inserts into one of the tunnels of the $1 \times 1 \times 2$ α-MnO_2 unit cell ($KMn_{16}O_{32}$), because of the electrostatic attraction from the K^+, the oxygen ligands of the [MnO_6] units will be pulled away from the central Mn. As density functional theory (DFT) calculated, the average bond length of [MnO_6] unit is increased from 1.90156 Å of bare α-MnO_2 to 1.905703 and 1.903862 Å for Mn1-O1/O2 and Mn2-O1/O2, respectively, for the α-MnO_2 with the K^+ insertion (Table S1, Supporting Information). Moreover, for the layer without the K^+ in the tunnel, the Mn1-O1/O2 bond length increases as large as 1.920743 Å (Table S2, Supporting Information). Due to the bond

length increase, the integral density of state (DOS) close to the Fermi level positively shift (Figure 2f), and more electron of Mn move to the conductive bond, resulting in the increase of the charge state of Mn by compared with pristine α-MnO_2.

Furthermore, the calculated Bader charge confirms the increase of the valence of Mn after the K^+ insertion (Table S3, Supporting Information). This verifies the binding energy increase of the Mn $2p_{3/2}$ and $2p_{1/2}$ XPS spectra of the as-prepared α-MnO_2 and Al-doped α-MnO_2 compared with commercial α-MnO_2 ($\approx$ 0.4 eV, as marked by the dashed line in Figure 2c). Meanwhile, the Bader charge is increased along with the bond length increase, explaining the multiple peaks of the Mn $2p_{3/2}$ XPS spectrum (as arrowed in the inset of Figure 2c). Figure S3 (Supporting Information) shows the XPS peak at $\approx$ 73.45 eV, in agreement with the position of the Al 2p peak, indicating that Al has been successfully doped.[28] Besides, both EDS and XPS quantify the atom ratio of doped Al which is also $\approx$10%, the same as the amount of the K^+ in the tunnel, revealing the Al doping principle. The inductively coupled plasma mass spectrometry (ICP-MS) technique (Table S4, Supporting Information) also results that the ratio of doped Al to Mn being 1:10. The K^+ in the precursor profits the bond length increase of Mn—O, weakening the bond energy between them. When Al was added to the precursor, due to the more strong bond energy between Al and O (502 kJ mol^{-1}) by compared with Mn and O (362 kJ mol^{-1}),[29,30] the trivalent aluminum ion is highly possible to substitute manganese in α-MnO_2 and forms a stable bond with the O atom. Furthermore, the DFT calculation indicates that the substitution doping of Al shows smaller formation energy than the interstitial doping. Furthermore, the interstitial doping of Al could form the readily localized DOS close to the Fermi level (Figure S4a, Supporting Information). However, no obvious XPS peak corresponding to such a feature can be observed (Figure 2b). Only the substitution doping feature (Figure S4b, Supporting Information) is presented, further confirming that Al doping is in the substitution manner. In addition, the XRD main peak (211) of Al-doped α-MnO_2 readily shifted to higher degrees of comparison with as-prepared pristine α-MnO_2 (Figure S5, Supporting Information). The rightward shift of the peak position indicates the lattice shrinkage, which is reasonable due to the shorter bond length between Al and O than that of Mn—O, further suggesting the substitution of Al. Furthermore, the intensity of the diffraction peak is weakened, suggesting the decrease in the particle size after the substitution of Al.[31,32] The ionic radius of Al^{3+} is smaller than that of the manganese ion, leading to a contraction in cell volume. The reduction in cell volume allows for stability during ion insertion and de-insertion, thus improving the electrochemical cycling stability of the sample (as shown later in the electrochemical tests).[33]

Surprisingly, by comparison with the high-resolution O 2p XPS spectrum of α-MnO_2, besides the main peak at 529.1 eV, a partial oxygen defect may be present with the substitutional doping of Al ions (Figure 2g).[34] Subsequently, based on this finding the electron paramagnetic resonance (EPR) technique was applied to test for oxygen defects in two samples. In contrast to α-MnO_2, the EPR curve for the Al-doped α-MnO_2 produced a stronger signal intensity at $g = 2.017$, which is indicative of the oxygen vacancies associated with the lattice (Figure 2h). It indicates that Al ion substitution doping indeed induces partial anion defects, providing more active sites for subsequent ion embedding.[35] Thereafter, the as-prepared Al-doped α-MnO_2 can be characterized as $Al_xK_yMnO_{2-z}$ (x = y = $\approx$ 10 a.t. %). Then the UV–Vis absorption spectra of α-MnO_2 and $Al_xK_yMnO_{2-z}$ were tested (Figure 2i). The results showed that both α-MnO_2 and $Al_xK_yMnO_{2-z}$ exhibited strong light absorption properties in the whole visible region. Among them, $Al_xK_yMnO_{2-z}$ shows a significant red shift in the visible region, indicating that Al substitution doping contributes to the light absorption ability.[36] In addition, the $Al_xK_yMnO_{2-z}$ light absorption effect is better than that of pure α-MnO_2.[37]

The morphologies of as-prepared pristine α-MnO_2 and $Al_xK_yMnO_{2-z}$ were characterized by Scanning Electron Microscopy (SEM) and Transmission Electron Microscopy (TEM). As shown in **Figure 3**, the as-prepared pristine α-MnO_2 presents the nanowires architecture (Figure 3a). The typical diameter of

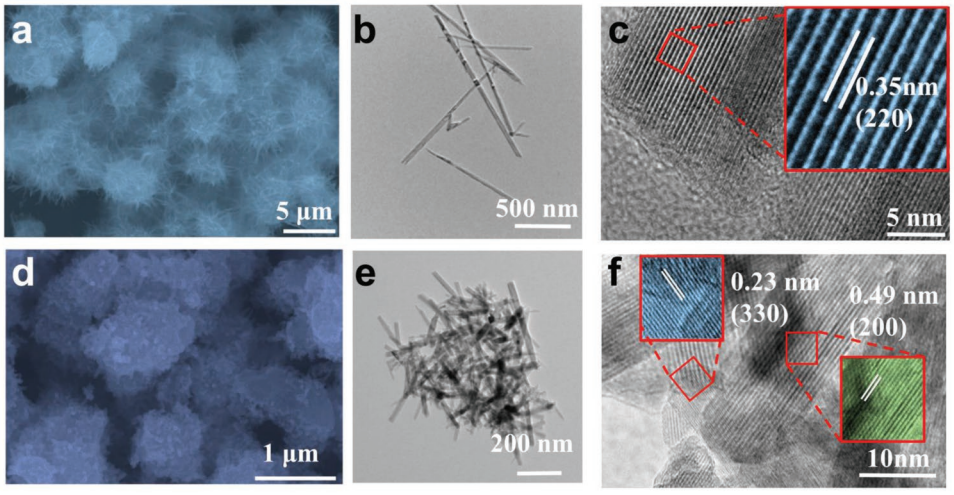

Figure 3. a) SEM image of α-MnO_2. b) TEM image of α-MnO_2. c) HRTEM of the as-prepared α-MnO_2. The inset of the HRTEM image shows the d-spacing of the as-prepared α-MnO_2. d) SEM image of $Al_xK_yMnO_{2-z}$. e) TEM image of $Al_xK_yMnO_{2-z}$. f) HRTEM of the as-prepared $Al_xK_yMnO_{2-z}$. The insets of HRTEM images show the d-spacing of the as-prepared $Al_xK_yMnO_{2-z}$.

a nanowire could be ≈ 50 nm (Figure 3b), with the high crystallinity feature as shown in the HRTEM image (Figure 3c). The inset of Figure 3c presents the *d*-spacing of the (220) crystal plane of the I4/m space group α-MnO_2. After doping with the Al, a large number of nanowires gradually aggregated as shown in the SEM image (Figure 3d). Due to the adoption of the hydrothermal preparation method, a slight agglomeration occurred, which is not conducive to our observation of the accurate morphology of the sample, so TEM characterization was further performed. The TEM image reveals its nanorod shape (Figure 3e). The diameter (≈40 nm) decreases a little compared with the pristine α-MnO_2 (≈ 50 nm). Besides, the typical pristine α-MnO_2 nanowire could be ≈ 1 µm in length. After doping, the length decreases a lot compared with the pristine α-MnO_2 (≈ 200 nm), which is consistent with the XRD change tendency. As identified by the HRTEM image (Figure 3f), the $Al_xK_yMnO_{2-z}$ preserves the great crystallinity feature. The (330) and (200) crystal planes with d-spacing of 0.23 and 0.49 nm, respectively, can be readily observed (insets in Figure 3f).[38]

The cyclic voltammetry (CV) curves for the first three cycles of $Al_xK_yMnO_{2-z}$ were first tested in a three-electrode cell with 0.5 M $MgSO_4$ aqueous solution as the electrolyte, graphite rods as counter electrodes, and Hg/HgO as the reference electrode with a scan rate of 0.2 mV s^{-1} (**Figure 4**a). In the first cycle, there is a fine oxidation peak at 0.95 V. However, its oxidation peak disappears from the second cycle onwards. To characterize

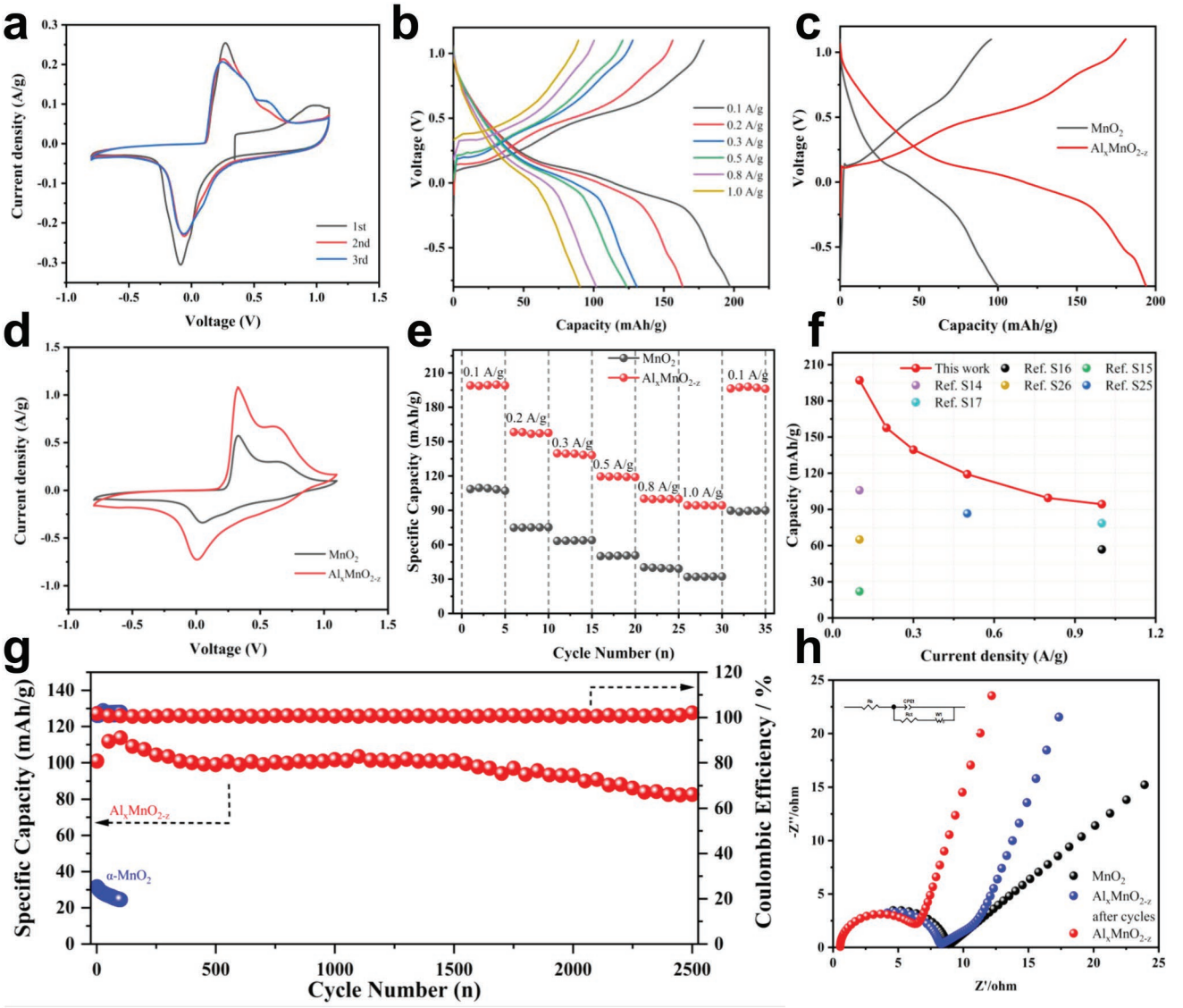

Figure 4. Electrochemical energy storage performance of Al_xMnO_{2-z} cathode in a three-electrode system. a) The CV curves at a scan rate of 0.2 mV s^{-1} for the first, second, and third cycles. b) GCD curves at different current densities from 0.1 to 1 A g^{-1}. c) Capacity comparison diagram of Al_xMnO_{2-z} and α-MnO_2 electrode materials at the current density of 0.1 A g^{-1}. d) CV curves of Al_xMnO_{2-z} and α-MnO_2 electrode materials at a scan rate of 1 mV s^{-1}. e) Rate performance at different specific currents for Al_xMnO_{2-z} and α-MnO_2 electrode materials. f) The capacity compared with other aqueous magnesium ion electrode materials. g) Long-term cycling performance and Coulombic efficiency of Al_xMnO_{2-z} and α-MnO_2 at 1 A g^{-1}. h) Nyquist plots of the Al_xMnO_{2-z} cathode before cycling, after 2500 cycles, and α-MnO_2 cathode before cycling.

this oxidization peak, the DFT was conducted to calculate the potential difference between the K^+ and Mg^{2+} extracted from the 1×1×2 α-MnO_2, as shown in Figure S6 (Supporting Information). The K^+ presents a 0.757 eV higher potential than the Mg^{2+} when extracted from the tunnel of $1 \times 1 \times 2$ α-MnO_2. Via the following CV oxidization curves, it can be identified that the Mg^{2+} has a 0.25 V oxidization peak. Therefore, the initial ≈ 0.95 V peak should be ascribed to that K ions within the tunnel in the $Al_xK_yMnO_{2-z}$ were extracted and dissolved in the electrolyte, due to the low concentration of K^+ in the 0.5 M $MgSO_4$ aqueous electrolyte, it hardly inserts back again during the following discharge process. Besides, the EDS mapping of $Al_xK_yMnO_{2-z}$ after cycles is shown in Figure S7a–e (Supporting Information). The element of O, Mn, and Al remained uniformly distributed in the material, whereas K was more dispersed than that before cycling. Furthermore, in order to further examine the K^+ gradual removal during the cycling process, the energy spectrum element content ratio under point scan was tested (Figure S7f, Supporting Information). The atomic ratio of doped aluminum after cycling is still ≈10%, which is consistent with that before cycling. In contrast, the content of K is negligible after cycles. Therefore, the oxidation peak at ≈ 0.95 V disappeared after the initial cycle. Then the electrode materials change to Al_xMnO_{2-z} and cycled for the rest cycles.[39] It shows a good overlap curve from the second cycle onwards, indicating good stability. The reduction peaks are at −0.06/0.10 V, and the oxidation peaks at 0.25/0.62 V overlap. This phenomenon is mainly due to the overpotential required for activation in the first cycle. The activation process narrows the potential window between oxidation and reduction, making the charge and discharge reversible.[40] The as-observed redox peaks in CV curves of the Al_xMnO_{2-z} sample corresponded to the redox process between Mn^{4+} and Mn^{3+}.[41] Subsequently, the constant current charging and discharging (GCD) curves of raw α-MnO_2 were compared under the same conditions to determine the superior performance of Al_xMnO_{2-z} (Figure 4b; Figure S8, Supporting Information). The GCD curves of Al_xMnO_{2-z} and α-MnO_2 at the current densities from 0.1 to 1 A g^{-1}. With the substitution doping of Al ions, the discharge plateau of the Al_xMnO_{2-z} electrode material is significantly higher than that of α-MnO_2 material. Furthermore, the charge-discharge curves can still easily distinguish the characteristic plateaus even at high current densities of 1 A g^{-1}. These results confirm the substitution doping of Al ions, which forms a more stable Al-O bond with higher performance and faster reaction kinetics.

In addition, Figure 4c clearly shows that Al_xMnO_{2-z} has a preferable reversible capacity of 197.02 and 100.54 mAh g^{-1} for α-MnO_2. Similarly, the CV curves of the two electrode materials were compared at a scan rate of 1 mV s^{-1} (Figure 4d). From the CV curves, it can be seen that Al_xMnO_{2-z} has a more pronounced redox peak, and its integral area also indicates that Al_xMnO_{2-z} has a higher specific capacity,[42] a result that is consistent with the GCD curves. Furthermore, the Electrostatic potential (ESP) diagrams of optimized (001) facets of Al_xMnO_{2-z} (Figure S9a, Supporting Information) and α-MnO_2 (Figure S9b, Supporting Information) were calculated. It shows that after doped with Al, the (001) facets present more negative charge (red colored region), profiting the electrostatic attraction with the Mg^{2+}. While due to the less electron density around the Al atom, the obvious electrophilic region formed (as arrowed in Figure S9, Supporting Information), which could result in the larger overpotential for the Al_xMnO_{2-z}. So this leads to a smaller polarization of α-MnO_2 samples than Al_xMnO_{2-z}. Immediately the rate performance of the two materials is compared, as shown in Figure 4e. Notably, the Al_xMnO_{2-z} electrode showed good rate performance, still providing a capacity of 90.50 mAh g^{-1} at a high current rate of 1 A g^{-1}. More specifically, the Al_xMnO_{2-z} electrode material has a higher capacity in aqueous Mg-ion batteries than most of the cathode materials described in the literature (Figure 4f) and the relevant literature is summarised in Table S5 (Supporting Information). To further demonstrate the substitution doping of Al to improve the stability of the material, the long-cycle performance of Al_xMnO_{2-z} and α-MnO_2 were compared (Figure 4g). After 2500 cycles, Al_xMnO_{2-z} still has a capacity retention rate of 82%, while α-MnO_2 drops to 77% after 100 cycles. In addition, electrochemical impedance spectroscopy (EIS) tests were carried out on both electrode materials before and after cycling (Figure 4h). The R_{ct} of the Al_xMnO_{2-z} before cycling is 7.3 Ω, and after 2500 cycles is 8.34 Ω. Meanwhile, the α-MnO_2 is also tested and the R_{ct} is 8.6 Ω. This suggests that the Al_xMnO_{2-z} cathode has a small interfacial charge transfer resistance and fast Mg^{2+} diffusion kinetics during the electrochemical reaction.

To further understand the electrochemical kinetics of the Al_xMnO_{2-z} and α-MnO_2 electrodes, CV measurements are carried out at various scan rates from 0.2 to 1.0 mV s^{-1}. Figure S10a (Supporting Information) shows the CV curves for Al_xMnO_{2-z} between −0.8 and 1.1 V at different scan rates. Two reduction peaks and two oxidation peaks are evident on each curve, which is consistent with the charge-discharge curve. Unlike normal ion diffusion, the square root of the peak current *(i)* is not well proportional to the scan rate *(v)*, suggesting that the charge-discharge process is composed of non-Faraday and Faraday behavior. According to previous studies, i and v are related by the following equation:[43]

$$i = av^b \tag{1}$$

that can be written as

$$\log(i) = b\log(v) + \log(a) \tag{2}$$

Where a and b are adjustable parameters. When b is equal to 1, the electrochemical system is controlled by capacitive. At a value of b of 0.5, ion diffusion dominates the charging and discharging process. Figure S10b (Supporting Information) shows the log(i) versus log(v) plots at the four reduction and oxidation peaks. Peaks 1, 2, 3, and 4 have b-values of 0.67, 0.74, 0.72, and 0.70 respectively, indicating contributions from both diffusive and capacitive processes. It leads to a fast Mg^{2+} insertion/extraction and persistent cycling stability. Similarly, kinetic analyses were carried out for α-MnO_2 (Figure S11a,b, Supporting Information). The CV curves both had four distinct redox peaks and all had b values between 0.5 and 1. It also represents that both diffusion-controlled faradaic processes and capacitive-controlled behaviors have synergetic effects on the electrochemical kinetics of the α-MnO_2 cathode.

The ratios of Mg^{2+} capacitive contribution can be further quantitatively quantified by separating the current response

i at a fixed potential V into capacitive effects (proportional to the scan rate v) and diffusion-controlled reactions ($k_2v^{1/2}$). The capacitive contribution can be calculated through the following equation:[44]

$$i = k_1v + k_2v^{1/2} \tag{3}$$

that can be portrayed as

$$i/v^{1/2} = k_1v^{1/2} + k_2 \tag{4}$$

At scan rates of 0.2, 0.4, 0.6, 0.8 and 1 mV s^{-1}, the capacitive and diffusion-controlled capacity values were 79%, 81%, 83%, 88% and 91% respectively (Figure S10c, Supporting Information). The results indicate that capacitive contribution dominates the total capacity and that capacitive contribution ratios increase gradually as the scan rate increases. Similarly, the capacitance contribution ratio of α-MnO_2 increases as the scan rate increases (Figure S11c, Supporting Information). In Figure S10d (Supporting Information), the voltage profiles of the capacitive currents (shaded areas) are compared with the total measured currents obtained at a scan rate of 1 mV s^{-1} for Al_xMnO_{2-z}. Also, Al_xMnO_{2-z} indicates a higher capacitive contribution ratio (91%) than the α-MnO_2 (80%) (Figure S11d, Supporting Information). These results may be attributed to Mg^{2+} interfacial absorption at the phase boundaries of Al_xMnO_{2-z}. In the meantime, the enhancement of the capacitive contribution of the Al_xMnO_{2-z} also accelerates Mg-ion diffusion kinetics significantly.

The Climbing Image-Nudged Elastic Band (CI-NEB) DFT calculation was also conducted for characterizing the Mg^{2+} diffusion barrier of the as-prepared Al-doped and oxygen defects α-MnO_2, Al_xMnO_{2-z}. As calculated above, the Mn1 site will be lengthened due to the K^+ insertion in the tunnel during the synthesis process, which is highly possible to be substituted by Al^{3+}. Therefore, as shown in **Figure 5**a,b, $1 \times 1 \times 2$ α-MnO_2 unit cell with two Mn1 sites substituted by Al was structured according to the X ratio within the as-prepared Al_xMnO_{2-z} sample. Meanwhile, the oxygen vacancies are considered here because the oxygen vacancies are highly possibly related to the substituted Al as revealed by the O 1s XPS and EPR (Figure 2g,h). After the relaxation, the DOS of the Al_xMnO_{2-z} shows the typical defect state near the Fermi level (Figure 5c), making the valence bond edge away from the Fermi level, which is consistent with the XPS spectrum (Figure 2b). The CI-NEB of Mg^{2+} diffusion along the tunnel of Al_xMnO_{2-z} and pristine α-MnO_2 was

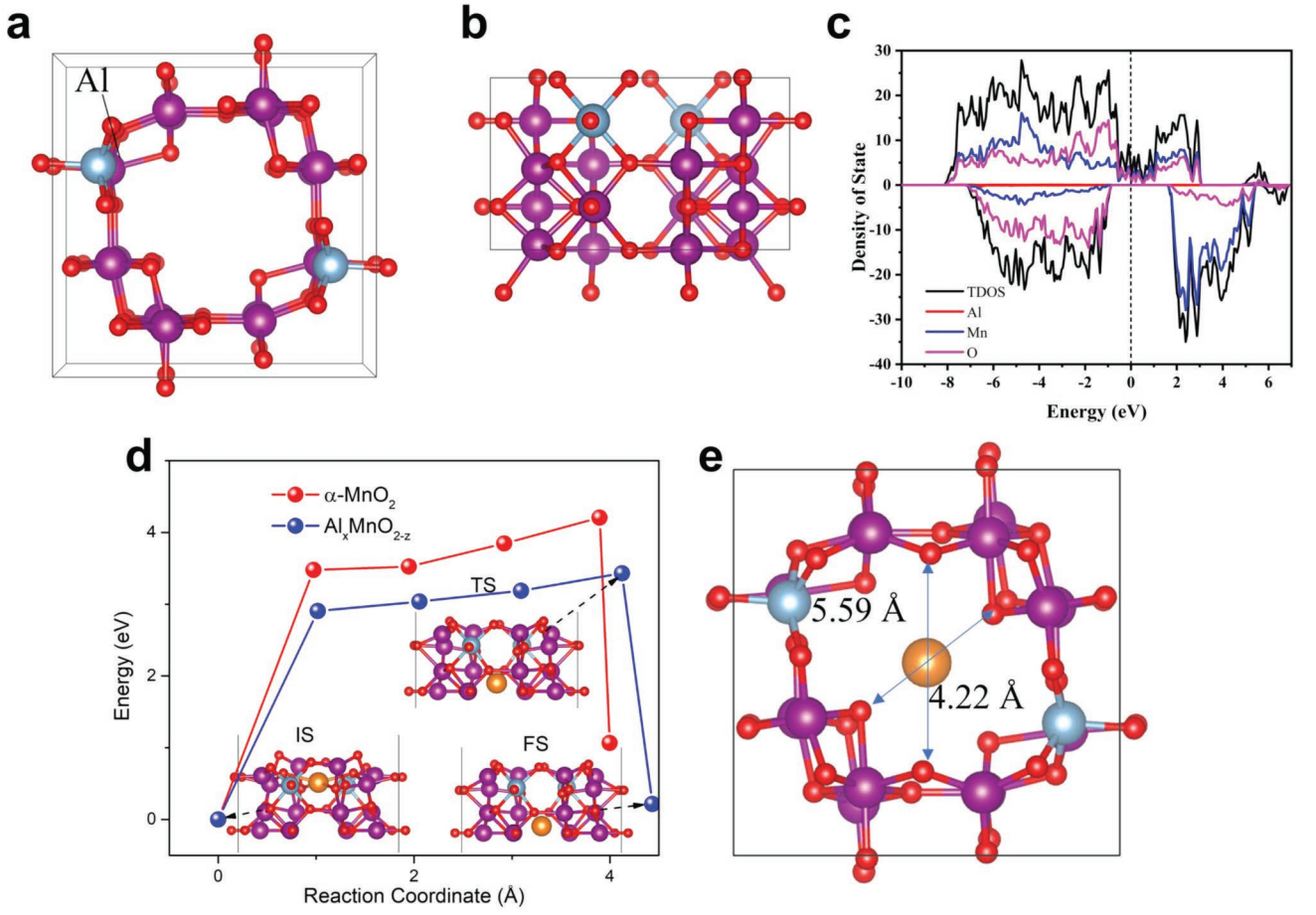

Figure 5. DFT relaxed structures along with c-axis a) and a-axis b) of Al_xMnO_{2-z}. c) is the density of state of the Al_xMnO_{2-z}. d) CI-NEB calculated the diffusion barrier of Mg^{2+} in the tunnels of Al_xMnO_{2-z} and pristine α-MnO_2. Inset is the a-axis view transition state of Mg^{2+} diffusion in the tunnels of Al_xMnO_{2-z}. e) c-axis view of the transition state of Mg^{2+} diffusion in the tunnels of Al_xMnO_{2-z}.

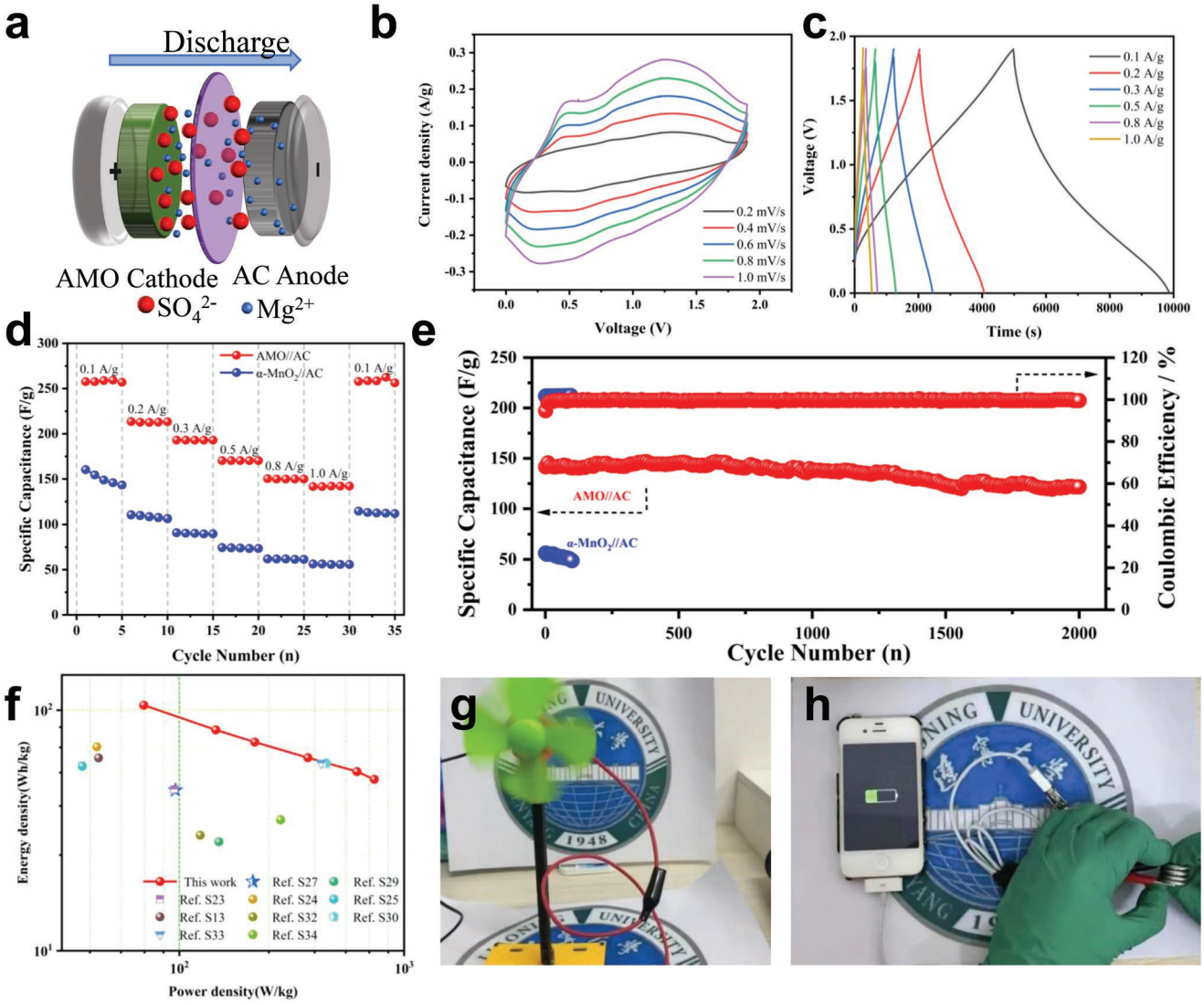

Figure 6. The aqueous AMO//AC Mg-ion capacitor system in 0.5 M $MgSO_4$ electrolyte. a) Schematic illustration of AMO//AC Mg-ion capacitor system. b) The CV curves. c) GCD curves at different current densities from 0.1 to 1 A g^{-1}. d) Rate performance at different specific currents for AMO//AC Mg-ion capacitor and α-MnO_2//AC Mg-ion capacitor. e) Long-term cycling performance and Coulombic efficiency of AMO//AC Mg-ion capacitor and α-MnO_2//AC Mg-ion capacitor at 1 A g^{-1}. f) The Ragone plots were compared with other aqueous magnesium ion devices and some aqueous zinc ion hybrid capacitors. g,h) Photographs of powering a small fan and a mobile phone.

calculated (Figure 5d,e). After Al substitution doping, the diffusion barrier decreased from 4.2 to 3.43 eV. The transition state is shown in the inset of Figure 5d. According to the trajectory images of the Mg^{2+} diffusion along the tunnel, the oxygens, electrostatic attracting Mg^{2+}, demonstrated the biggest movements (Figure S12a, Supporting Information). By comparing the distance between the oxygen atoms coordinated with Mg^{2+} at the transition state, the value decreases from 4.26 (O2-O2), 5.68 (O1-O1) Å of pristine α-MnO_2 (Figure S12b, Supporting Information) to 4.22 and 5.59 Å of Al_xMnO_{2-z} (Figure 5e), it concludes that after doping with Al, oxygens distance shortening benefits the electrostatic attracting of Mg^{2+} cations and decreases the Mg^{2+} diffusion barrier.

To demonstrate the application of the Al_xMnO_{2-z} electrode, an Mg-ion capacitor (MIC) has been fabricated using activated carbon (AC) and Al_xMnO_{2-z} as the anode and cathode, respectively. According to the mass ratios of cathode versus anode, they were calculated to be about Al_xMnO_{2-z} : AC = 1:7.8, and α-MnO_2 : AC = 1:5.9, respectively. The schematic diagram in **Figure 6**a illustrates the configuration of the Al_xMnO_{2-z}// AC (AMO//AC) MIC. As a comparison, the α-MnO_2//AC MIC was assembled in the same way. Subsequently, electrochemical tests were carried out on both devices. Figure 6b shows the CV curves for AMO//AC at scan rates of 0.2–1 mV s^{-1} with a voltage window of 0–1.9 V. The charge storage mechanisms of MIC are demonstrated by the near-rectangular shapes of CV curves, which are contributed by a combination of faradaic and nonfaradaic reactions. Even at 1 mV s^{-1}, the CV shape is well retained, indicating that the MIC has a good rate capability. Meanwhile, compared with α-MnO_2//AC MIC (Figure S13a,

Supporting Information), AMO//AC MIC shows a larger CV area, revealing a higher capacity. Figure 6c shows the GCD curves of the AMO//AC MIC at different current densities. The triangular shape of the curves is well maintained with good reversibility as the current density increases. This once again reveals the interfacial electrochemical reaction with rapid energy storage kinetics. The GCD curves of α-MnO_2//AC also show reversibility in Figure S13b (Supporting Information). After that, the rate performance of the AMO//AC MIC and α-MnO_2//AC MIC at current densities of 0.1–1 A g^{-1} is shown in Figure 6d. The specific capacitance of the AMO//AC MIC was calculated to be 259.26, 213.47, 192.95, 170.26, 150.31, and 142.10 F g^{-1} at current densities of 0.1–1 A g^{-1}, respectively. While the specific capacitance of the α-MnO_2//AC MIC is 148.84, 108.42, 90.15, 74.47, 61.89, and 56.31 F g^{-1} for the same current density. At high current densities of 1 A g^{-1}, the specific capacitance increases by a factor of ≈2.5. In addition, for a ten-fold increase in current density (from 0.1 to 1 A g^{-1}), the specific capacitance retention of this AMO//AC MIC can still reach 46%, which is higher than 33% of that of α-MnO_2//AC MIC. Furthermore, for the as-prepared AMO//AC MIC and α-MnO_2//AC MIC, long cycling tests to verify cycling life were conducted. As shown in Figure 6e, the AMO//AC MIC exhibited 86% capacitance retention and kept 100% Coulombic efficiency for 2000 cycles. However, α-MnO_2//AC is already down to 86% capacitance retention after just 100 cycles. The robust cycling performance is due to the Al-O bonding strategy with Al substitution doping, which improves reaction kinetics and reduces migration difficulty and structural stability. The energy and power densities of the AMO//AC MIC are determined using Equations (5) and (6) (Supporting Information). A high energy density of 104.86 Wh kg^{-1} can be achieved at a power density of 69.44 W kg^{-1}. Even at a high power density of 736.71 W kg^{-1}, a decent energy density of 51.57 Wh kg^{-1} can be achieved. In addition, the excellent energy–power characteristics of our MIC are remarkably better than that of recently reported Mg-ion devices and other aqueous zinc ion hybrid capacitors (Figure 6f, the related data are listed in Table S6, Supporting Information). For the practical application, two AMO//AC MIC connected in series could successfully spin a fan (Figure 6g), while four-coin cells connected in series also successfully charged a mobile phone (Figure 6h), suggesting that the device has promising applications.

To further visualize the difference in electrochemical kinetics between AMO//AC and α-MnO_2//AC, EIS and the galvanostatic intermittent titration technique (GITT) tests were performed.[45,46] By comparing the EIS results before and after the cycling of the two capacitors, the R_{ct} value of the AMO//AC was determined to be 4.21 Ω, which is significantly smaller than that of the original α-MnO_2//AC (5.59 Ω), indicating that the conductivity-enhanced Al_xMnO_{2-z} cathode significantly promotes the charge transfer capability (Figure S14, Supporting Information). The GITT test in Figure S15a,b (Supporting Information) also verifies this opinion. The D_{Mg2+} value of AMO//AC is calculated to be 5.70×10^{-11} and 1.02×10^{-13}, impressively, higher than that of α-MnO_2//AC (3.55×10^{-11}–1.32×10^{-14} cm^2 s^{-1}). The substitutional doping of aluminum ions facilitates the rapid diffusion of magnesium ions during the insertion/extraction process, thus increasing the D value of Mg^{2+}. The results show that the AMO//AC has a small interfacial charge transfer resistance and fast Mg^{2+} diffusion kinetics. This well explains the increased capacity, cycling stability, and rate performance of the AMO//AC.

3. Conclusions

To summarize, we constructed a novel Mg-ion capacitor with Al_xMnO_{2-z} as the cathode and active carbon as the anode in an aqueous electrolyte. The substitution doping of Al has been theoretically and technically demonstrated to be of great superiority for material property modification. The Al_xMnO_{2-z} has a specific capacity of 197.02 mAh g^{-1} in the three-electrode system. Furthermore, the MIC assembled with the AC anode provided a high specific capacitance of 259.26 F g^{-1} and long cycling durability of 2000 cycles with 86% capacitance retention. In combination with CI-NEB DFT calculation, we proved that the K^+ in the precursor favors the increase of the bond length of Mn—O, weakening the bond energy between them and favoring the Al^{3+} substitution doping. Moreover, the partial substitution of doped Al reduces the diffusion potential of Mg^{2+} in the Mn lattice. Our research shows that using a cathode with high electrochemical kinetics to build high-performance Mg-ion capacitors for large-scale and rapid energy storage and conversion is a crucial and powerful strategy.

Supporting Information

Supporting Information is available from the Wiley Online Library or from the author.

Acknowledgements

This work was supported by the National Natural Science Foundation of China (No. 52071171, 52202248), Liaoning Revitalization Talents Program – Pan Deng Scholars (XLYC1802005), Liaoning BaiQianWan Talents Program (LNBQW2018B0048), Natural Science Fund of Liaoning Province for Excellent Young Scholars (2019-YQ-04), Key Project of Scientific Research of the Education Department of Liaoning Province (LZD201902), Shenyang Science and Technology Project (21-108-9-04), the Research Fund for the Doctoral Program of Liaoning Province (2022-BS-114), Australian Research Council (ARC) through Future Fellowship (FT210100298), Discovery Project (DP220100603), and Linkage Project (LP210200504) schemes, CSIRO Energy Centre and Kick-Start Project. The Study Melbourne Research Partnerships program had been made possible by funding from the Victorian Government through Study Melbourne.

Open access publishing facilitated by RMIT University, as part of the Wiley - RMIT University agreement via the Council of Australian University Librarians.

Conflict of Interest

The authors declare no conflict of interest.

Data Availability Statement

The data that support the findings of this study are available from the corresponding author upon reasonable request.

Keywords

Al substitutions, aqueous Mg-ion capacitors, electrochemical energy storage, locally tuned structures

Received: September 9, 2022
Revised: October 9, 2022
Published online: October 31, 2022

[1] T. D. Gregory, R. J. Hoffman, R. C. Winterton, *J. Electrochem. Soc.* **1990**, *137*, 775.
[2] Y. Zhang, K. Cheng, K. Ye, Y. Gao, W. Zhao, G. Wang, D. Cao, *Electrochim. Acta* **2015**, *182*, 971.
[3] Z. Wang, Q. Su, J. Shi, H. Deng, G. Q. Yin, J. Guan, M. P. Wu, Y. L. Zhou, H. L. Lou, Y. Q. Fu, *ACS Appl. Mater. Interfaces* **2014**, *6*, 6786.
[4] J. Xie, C. Li, Z. Cui, X. Guo, *Adv. Funct. Mater.* **2015**, *25*, 6519.
[5] K. W. Nam, S. Kim, S. Lee, M. Salama, I. Shterenberg, Y. Gofer, J. S. Kim, E. Yang, C. S. Park, J. S. Kim, S. S. Lee, W. S. Chang, S. G. Doo, Y. N. Jo, Y. Jung, D. Aurbach, J. W. Choi, *Nano Lett.* **2015**, *15*, 4071.
[6] X. Bie, K. Kubota, T. Hosaka, K. Chihara, S. Komaba, *J. Mater. Chem. A* **2017**, *5*, 4325.
[7] S. Gheytani, Y. Liang, F. Wu, Y. Jing, H. Dong, K. K. Rao, X. Chi, F. Fang, Y. Yao, *Adv. Sci.* **2017**, *4*, 1700465.
[8] C. Yuan, Y. Zhang, Y. Pan, X. Liu, G. Wang, D. Cao, *Electrochim. Acta* **2021**, *385*, 138447.
[9] J. Niu, Z. Zhang, D. Aurbach, *Adv. Energy Mater.* **2020**, *10*, 2000697.
[10] Z. Guo, S. Zhao, T. Li, D. Su, S. Guo, G. Wang, *Adv. Energy Mater.* **2020**, *10*, 1903591.
[11] M. J. Deng, J. K. Chang, C. C. Wang, K. W. Chen, C. M. Lin, M. T. Tang, J. M. Chen, K. T. Lu, *Energy Environ. Sci.* **2011**, *4*, 3942.
[12] J. Z. Yang, B. S. Yin, Y. Sun, H. G. Pan, W. P. Sun, B. H. Jia, S. W. Zhang, T. Y. Ma, *Nano-Micro Lett.* **2022**, *14*, 42.
[13] Y. Ding, X. Shen, S. Sithambaram, S. Gomez, R. Kumar, V. M. B. Crisostomo, S. L. Suib, M. Aindow, *Chem. Mater.* **2005**, *17*, 5382.
[14] Y. J. Ren, F. B. Meng, S. W. Zhang, B. Ping, H. Li, B. S. Yin, T. Y. Ma, *Carbon Energy* **2022**, *3*, 446.
[15] S. W. Zhang, B. S. Yin, C. Liu, Z. B. Wang, D. M. Gu, *Chem. Eng. J.* **2017**, *312*, 296.
[16] G. Fang, C. Zhu, M. Chen, J. Zhou, B. Tang, X. Cao, X. Zheng, A. Pan, S. Liang, *Adv. Funct. Mater.* **2019**, *29*, 1808375.
[17] H. Pan, Y. Shao, P. Yan, Y. Cheng, K. S. Han, Z. Nie, C. Wang, J. Yang, X. Li, P. Bhattacharya, K. T. Mueller, J. Liu, *Nat. Energy* **2016**, *1*, 16039.
[18] H. Zhang, J. Wang, Q. Liu, W. He, Z. Lai, X. Zhang, M. Yu, Y. Tong, X. Lu, *Energy Storage Mater.* **2019**, *21*, 154.
[19] S. Zhang, N. Pan, *Adv. Energy Mater.* **2015**, *5*, 1401401.
[20] H. Wang, R. Gao, Z. Li, L. Sun, Z. Hu, X. Liu, *Inorg. Chem.* **2018**, *57*, 5249.
[21] C. Chen, M. Shi, Y. Zhao, C. Yang, L. Zhao, C. Yan, *Chem. Eng. J.* **2021**, *422*, 130375.
[22] Y. Huang, W. He, P. Zhang, X. Lu, *Funct. Mater. Lett.* **2018**, *11*, 1840006.
[23] X. Chen, C. Long, C. Lin, T. Wei, J. Yan, L. Jiang, Z. Fan, *Electrochim. Acta* **2014**, *137*, 352.
[24] J. Huang, J. Wei, Y. B. Xiao, Y. Xu, Y. J. Xiao, Y. Wang, L. Tan, K. Yuan, Y. Chen, *ACS Nano* **2018**, *12*, 3030.
[25] Q. Chen, J. Jin, Z. Kou, C. Liao, Z. Liu, L. Zhou, J. Wang, L. Mai, *Small* **2020**, *16*, 2000091.
[26] M. Yu, Y. Han, X. Cheng, L. Hu, Y. Zeng, M. Chen, F. Cheng, X. Lu, Y. Tong, *Adv. Mater.* **2015**, *27*, 3085.
[27] T. Zhai, X. Lu, Y. Ling, M. Yu, G. Wang, T. Liu, C. Liang, Y. Tong, Y. Li, *Adv. Mater.* **2014**, *26*, 5869.
[28] M. Xu, N. Fu, X. Wang, Z. Yang, *J. Mater. Sci. Mater. Electron.* **2020**, *31*, 16027.
[29] Q. Xie, Z. Cai, P. Li, D. Zhou, Y. Bi, X. Xiong, E. Hu, Y. Li, Y. Kuang, X. Sun, *Nano Res.* **2018**, *11*, 4524.
[30] R. A. Davoglio, G. Cabello, J. F. Marco, S. R. Biaggio, *Electrochim. Acta* **2018**, *261*, 428.
[31] X. Zeng, B. Li, R. Liu, X. Li, T. Zhu, *Chem. Eng. J.* **2020**, *384*, 123362.
[32] Q. Xie, Z. Cai, P. Li, D. Zhou, Y. Bi, X. Xiong, E. Hu, Y. Li, Y. Kuang, X. Sun, *Nano Res.* **2018**, *11*, 4524.
[33] E. Iwata, K. Takahashi, K. Maeda, T. Mouri, *J. Power Sources* **1999**, *81–82*, 430.
[34] Q. Tan, X. Li, B. Zhang, X. Chen, Y. Tian, H. Wan, L. Zhang, L. Miao, C. Wang, Y. Gan, J. Jiang, Y. Wang, H. Wang, *Adv. Energy Mater.* **2020**, *10*, 2001050.
[35] J. Wang, J. G. Wang, X. Qin, Y. Wang, Z. You, H. Liu, M. Shao, *ACS Appl. Mater. Interfaces* **2020**, *12*, 34949.
[36] H. Shen, D. Shang, L. Li, D. Li, W. Shi, *Appl. Surf. Sci.* **2022**, *578*, 152024.
[37] X. Zhang, J. Ma, C. Fan, M. Peng, S. Komarneni, *J. Alloys Compd.* **2019**, *785*, 343.
[38] N. Jabeen, Q. Xia, S. V. Savilov, S. M. Aldoshin, Y. Yu, H. Xia, *ACS Appl. Mater. Interfaces* **2016**, *8*, 33732.
[39] N. Zarshad, A. U. Rahman, J. Wu, A. Ali, F. Raziq, L. Han, P. Wang, G. Li, H. Ni, *Chem. Eng. J.* **2021**, *415*, 128967.
[40] D. Wang, L. Wang, G. Liang, H. Li, Z. Liu, Z. Tang, J. Liang, C. Zhi, *ACS Nano* **2019**, *13*, 10643.
[41] T. H. Lee, D. T. Pham, R. Sahoo, J. Seok, T. H. T. Luu, Y. H. Lee, *Energy Storage Mater.* **2018**, *12*, 223.
[42] S. W. Zhang, B. S. Yin, Y. Z. Luo, L. Shen, B. S. Tang, Z. Kou, X. Liu, D. B. K. Lim, D. M. Gu, Z. B. Wang, H. Gong, *Nano Energy* **2020**, *68*, 104314.
[43] K. Zhang, M. Park, L. Zhou, G. H. Lee, W. Li, Y. M. Kang, J. Chen, *Adv. Funct. Mater.* **2016**, *26*, 6728.
[44] D. Chao, C. Zhu, P. Yang, X. Xia, J. Liu, J. Wang, X. Fan, S. V. Savilov, J. Lin, H. J. Fan, Z. X. Shen, *Nat. Commun.* **2016**, *7*, 12122.
[45] X. Zhu, Z. Cao, X. L. Li, L. Pei, J. Jones, Y. N. Zhou, P. Dong, L. Wang, M. Ye, J. Shen, *Energy Storage Mater.* **2022**, *45*, 568.
[46] Y. Li, X. Li, H. Duan, S. Xie, R. Dai, J. Rong, F. Kang, L. Dong, *Chem. Eng. J.* **2022**, *441*, 136008.